MAX-PLANCK-INSTITUT FÜR PLASMAPHYSIK

GARCHING BEI MÜNCHEN

Axisymmetric MHD Equilibria with Flow

W. Kerner

O. Jandl

IPP 6/230
IPP 1/220

August 1983

Die nachstehende Arbeit wurde im Rahmen des Vertrages zwischen dem Max-Planck-Institut für Plasmaphysik und der Europäischen Atomgemeinschaft über die Zusammenarbeit auf dem Gebiete der Plasmaphysik durchgeführt.

IPP 6/230
1/220

W. Kerner
O. Jandl

Axisymmetric MHD Equilibria with Flow

August 1983 (in English)

Abstract

Axisymmetric, ideal MHD configurations with steady flow are computed by applying the finite element method. Rectangular elements with four to eight nodes are used. By mesh rearrangement the equilibria are obtained in flux coordinates. Accurate results without flow and with purely toroidal flow are presented.

0. Introduction

The existence of an MHD equilibrium is considered as a necessary condition for the successful operation of a tokamak. Assuming isotropic pressure yields the well-known Grad-Schlüter-Shafranov equation for axisymmetric configurations. This nonlinear equation is usually solved numerically to allow arbitrary plasma shapes and current profiles. Such codes are in permanent use for control and analysis of operating experiments and for designing new devices.

Present experiments use large auxiliary heating power in the form of neutral beam injection to increase the plasma temperature substantially. This injection creates a flow in the plasma, in both the toroidal and poloidal directions. The toroidal flow velocities become comparable to the ion sound speed, as has been observed in experiments. The poloidal flow appears to be damped so that large poloidal flow velocities have not yet been observed. Enlarged transport due to non-uniform pressure and density on a flux surface is responsible for such damping. The neutral-beam-driven rotation of the plasma may therefore result in the deterioration of the energy confinement observed in experiments.

In order to describe plasmas with flow, the inertia term $\varrho \underline{u} \cdot \nabla \underline{u}$ has to be taken into account in the momentum equation. If the flow is purely toroidal, the resulting equation is basically the Grad-Schlüter-Shafranov equation.

Existing codes are thus easily extended for this case. It is our opinion that poloidal flow is interesting, even if it is not observed directly, because it causes a poloidal dependence of pressure and density on magnetic surfaces. Such profiles should be of great interest for transport theory and simulation! In this case the resulting equations become more complicated and require special treatment.

The Galerkin method in conjunction with finite elements is used for the numerical solution. This method closely resembles the variational formulation of the problem. The finite element method is completely general with respect to the geometry of the plasma cross-section and arbitrary boundary conditions. In addition, the elements can be arranged in the iteration process to coincide with the surfaces of constant flux. In this manner the equilibrium is obtained in adapted coordinates without working directly in flux coordinates.

The paper is organized in the following way: The physical model and the equilibrium equations are discussed in Sec. I. The numerical method and the code are described in Sec. II. Section III presents the results. The discussion and conclusion are given in Sec. IV.

1. Physical Model

We begin with the ideal MHD equations for the density ϱ, the velocity $\underline{u}$, the scalar pressure p and the magnetic field $\underline{B}$:

Continuity: $$\frac{\partial}{\partial t}\varrho + \nabla\cdot(\varrho\underline{u}) = 0 \qquad (1)$$

Momentum: $$\varrho\left(\frac{\partial}{\partial t} + \underline{u}\cdot\nabla\right)\underline{u} = -\nabla p + \underline{j}\times\underline{B} \qquad (2)$$

Maxwell-Ohm: $$\frac{\partial}{\partial t}\underline{B} = \nabla\times(\underline{u}\times\underline{B}) \qquad (3)$$

Maxwell: $$\nabla\cdot\underline{B} = 0 \qquad (4)$$

$$\underline{j} = \nabla\times\underline{B} \qquad (5)$$

The absence of any dissipation is expressed by the conservation of the entropy S:

$$\left(\frac{\partial}{\partial t} + \underline{u}\cdot\nabla\right)S = 0 \qquad (6)$$

The plasma is assumed to be an ideal gas, i.e.

$$p = T\varrho \qquad (7)$$

T being the temperature.

The thermodynamic relations lead to the caloric equation of state /1/:

$$p = S\,\varrho^{\gamma} \qquad (7a)$$

where γ is the ratio of specific heats, which is taken as equal to 5/3, as usual.

To compute axisymmetric equilibria we work in usual cylindrical coordinates r,θ,z, with θ being the ignorable coordinate.

The stationary, i.e. $\frac{\partial}{\partial t}=0$, equations read

$$\nabla(\rho \underline{u}) = 0 \tag{8}$$

$$\rho(\underline{u}\cdot\nabla)\underline{u} = -\nabla p + (\nabla\times\underline{B})\times\underline{B} \tag{9}$$

$$\nabla\times(\underline{u}\times\underline{B}) = 0 \tag{10}$$

$$\nabla\cdot\underline{B} = 0 \tag{11}$$

$$(\underline{u}\cdot\nabla)S = 0 \tag{12}$$

$$p = S\rho^{\gamma} \tag{13}$$

The equations for equilibria with flow were first derived by Zehrfeld and Green /2/. Here we closely follow a more recent derivation by Hameiri /3/.

The magnetic field is represented as

$$\underline{B} = \nabla\theta\times\nabla\Psi + F\nabla\theta \tag{14}$$

where Ψ is the poloidal flux and F the poloidal current profile.

The velocity can be decomposed into a toroidal component and one along $\underline{B}$ (poloidal)

$$\underline{u} = \frac{1}{\rho}\Phi(\Psi)\underline{B} + \frac{\Omega(\Psi)}{|\nabla\theta|^2}\nabla\theta \ , \tag{15}$$

where Φ and Ω are functions of Ψ alone. Furthermore, the entropy

is also a surface quantity

$$S = S(\Psi) \tag{16}$$

The components of the velocity and the field are restricted by the identity

$$F = \frac{I(\Psi) + \Phi\,\Omega/|\nabla\theta|^2}{1 - \Phi^2/\varrho} \tag{17}$$

where $I = I(\Psi)$ is a surface quantity. In the case with no poloidal flow, i.e. $\Phi = 0$, this identity gives $F = F(\Psi)$.

A second identity involves the entropy

$$H(\Psi) = \frac{\Phi^2}{2\varrho^2}\,\underline{B}^2 - \frac{\Omega^2}{2|\nabla\theta|^2} + \frac{\gamma}{\gamma-1}\,S(\Psi)\,\varrho^{\gamma-1} \tag{18}$$

where $H = H(\Psi)$ is a free surface quantity.

The radial ($\nabla\Psi$) component of the momentum equation yields

$$\nabla\left[\left(1 - \frac{\Phi^2}{\varrho}\right)|\nabla\theta|^2\,\nabla\Psi\right] + \underline{u}\cdot\underline{B}\,\frac{d\Phi}{d\Psi} + \varrho\left(\frac{\Omega}{|\nabla\theta|^2} + \frac{F\cdot\Phi}{\varrho}\right)\frac{d\Omega}{d\Psi} + \tag{19}$$

$$+ |\nabla\theta|^2\,F\,\frac{dI}{d\Psi} + \varrho\,\frac{dH}{d\Psi} - \frac{1}{\gamma-1}\,\varrho^{\gamma}\,\frac{dS}{d\Psi} = 0$$

The plasma is assumed to be confined within a toroidal, rigid perfect conductor with the boundary conditions of zero normal components of $\underline{u}$ and $\underline{B}$ at the wall. We can specify the five surface quantities Φ, Ω, I, H and S arbitrarily, as well as the plasma cross-section. The functions F and ϱ are, in general, not surface quantities. Together with the partial differential equation (19) the two algebraic

equations (17) and (18) have to be satisfied. Equation (18) contains the information that ϱ is a function of $|\nabla\psi|^2$. To be more precise one has

$$\varrho = \varrho(r, \psi, |\nabla\psi|^2) \tag{20}$$

Closer inspection of the differential equation (19) reveals that the type of the equation is defined by the second derivatives, i.e. by the term

$$\nabla\left[\left(1 - \frac{\Phi^2}{\varrho}\right) |\nabla\theta|^2 \nabla\psi\right] \tag{21}$$

Using the relation (20), it is seen that the highest derivatives are due to

$$\left(1 - \frac{\Phi^2}{\varrho}\right) \Delta\psi + \frac{\Phi^2}{\varrho^2} \nabla\psi \cdot \nabla\varrho$$

where

$$\nabla\psi \cdot \nabla\varrho = \frac{\partial\varrho}{\partial r} \nabla\psi \cdot \nabla r + \frac{\partial\varrho}{\partial\psi} \nabla\psi \cdot \nabla\psi + \frac{\partial\varrho}{\partial|\nabla\psi|^2} \nabla\psi \cdot \nabla|\nabla\psi|^2$$

It is convenient to normalize the velocity along $\underline{B}$ (poloidal component) to the poloidal Alfvén velocity

$$A = \Phi / \sqrt{\varrho} \tag{22}$$

The analysis shows that the differential equation (19) is elliptical if

$$0 \leq A^2 \leq \beta \tag{23a}$$

where the plasma beta is defined as

$$\beta = \frac{\gamma p}{\gamma p + \underline{B}^2}$$

For a value of beta between 1 and 10% the normalized velocity A is small, $A \lesssim 0.1 - 0.3$. The differential equation is of hyperbolic type if

$$\beta \leq A^2 \leq A_s^2 \tag{23b}$$

again of elliptical type if

$$A_s^2 \leq A^2 \leq A_f^2 \tag{23c}$$

and again of hyperbolic type if

$$A_f^2 \leq A^2 \tag{23d}$$

A_s^2 and A_f^2 corresponding to the slow and fast compressive waves are defined (see Ref. /3/) as:

$$A_s^2 = 1 - \left[1 - 4\beta B_p^2 / (\underline{B}^2 + \gamma p)\right]^{1/2} (\underline{B}^2 + \gamma p)/2B_p^2 ,$$

$$A_f^2 = 1 + \left[1 - 4\beta B_p^2 / (\underline{B}^2 + \gamma p)\right]^{1/2} (\underline{B}^2 + \gamma p)/2B_p^2 ,$$

where $B_p^2 = |\nabla\psi|^2 |\nabla\theta|^2$

For small poloidal velocities (eq. 23a) the flow is strictly elliptic. There are then no additional difficulties to solve the algebraic equations (18) and (17), as can be seen from the theory of implicit functions.

If the poloidal flow is in the range of eq. 23b, the differential equation is of hyperbolic type. Shock waves then have to be expected, which may cause changes in the topology. The algebraic equations 17 and 18 may then impose additional constraints on the solution, as discussed in Ref. /2/. In the introduction we pointed out that it should be interesting to study large poloidal flow and the resulting poloidal variation for ϱ and p. We thus have to be prepared for the transition from elliptic to hyperbolic type in the numerical solution.

With the transformation used in Ref. /4/

$$\begin{aligned} \tilde{\varrho} &= S^{1/\gamma}\varrho \\ \tilde{\Omega} &= S^{-1/2\gamma}\Omega \\ \tilde{\Phi} &= S^{1/2\gamma}\Phi \end{aligned} \tag{24}$$

we can eliminate the entropy. The equations using the fact that $\tilde{\underline{B}} = \underline{B}$, $\tilde{\underline{u}} = S^{-1/2\gamma}\underline{u}$ and $\tilde{H} = HS^{-1/\gamma}$ read

$$F = \frac{1 + \tilde{\Omega}\tilde{\Phi}/|\nabla\theta|^2}{1 - \tilde{\Phi}^2/\tilde{\varrho}} \,, \tag{17b}$$

$$\tilde{H} = \frac{\tilde{\Phi}^2}{2\tilde{\varrho}^2}\underline{B}^2 - \frac{\tilde{\Omega}^2}{2|\nabla\theta|^2} + \frac{\gamma}{\gamma-1}\tilde{\varrho}^{\gamma-1} \tag{18b}$$

$$\begin{aligned} &\nabla\left[\left(1-\frac{\tilde{\Phi}^2}{\tilde{\varrho}^2}\right)|\nabla\theta|^2\nabla\psi\right] + \tilde{\underline{u}}\cdot\underline{B}\,\frac{d\tilde{\Phi}}{d\psi} + \\ &+ \tilde{\varrho}\left(\frac{\tilde{\Omega}}{|\nabla\theta|^2} + \frac{F\tilde{\Phi}}{\tilde{\varrho}}\right)\frac{d\tilde{\Omega}}{d\psi} + |\nabla\theta|^2 F\frac{dI}{d\psi} + \tilde{\varrho}\frac{d\tilde{H}}{d\psi} = 0 \end{aligned} \tag{19b}$$

A solution of the equations (17b - 19b), i.e. $S \equiv 1$, together with four arbitrary functions $\tilde{\Phi}$, $\tilde{\Omega}$, $\tilde{I}$ and $\tilde{H}$ generates with the transformation (24) a family of new equilibria with profiles $S = S(\psi)$.

Purely toroidal flow:

We now discuss the special case of zero poloidal flow, i.e. $\tilde{\Phi}(\psi) \equiv 0$. Equation (17) gives $F = I(\psi)$. The Bernoulli-type equation (18) reads

$$\frac{\gamma}{\gamma-1}S\varrho^{\gamma-1} - \frac{\Omega^2}{2|\nabla\theta|^2} = i - \frac{\Omega^2}{2|\nabla\theta|^2} = H(\psi) \tag{25}$$

where i is the specific enthalpy.

The differential equation (19) takes the form

$$\nabla\left(|\nabla\theta|^2\,\nabla\psi\right) + \frac{\varrho\,\Omega}{|\nabla\theta|^2}\frac{d\Omega}{d\psi} + |\nabla\theta|^2 F\frac{dF}{d\psi} + \varrho\frac{dH}{d\psi} - \frac{\varrho^{\gamma}}{\gamma-1}\frac{dS}{d\psi} = 0$$

From eq. (25) we obtain for $S \neq 0$

$$\varrho^{\gamma-1} = \left(H(\psi) + \frac{\Omega^2}{2|\nabla\theta|^2}\right)\frac{\gamma-1}{S\gamma}$$

and further

$$\nabla\left(|\nabla\theta|^2\nabla\psi\right) + |\nabla\theta|^2\frac{dF}{d\psi} + \left[\left(H + \frac{\Omega^2}{2|\nabla\theta|^2}\right)\frac{\gamma-1}{S\gamma}\right]^{1/(\gamma-1)} \cdot \left\{\Omega\frac{1}{|\nabla\theta|^2}\frac{d\Omega}{d\psi} + \frac{dH}{d\psi} - \frac{1}{S\varrho}\left(H + \frac{\Omega^2}{2|\nabla\theta|^2}\right)\frac{dS}{d\psi}\right\} = 0 \qquad (26)$$

This equation contains four arbitrary functions F, Ω, H and S. If these functions and the boundary condition for Ψ are specified, the solution of the problem is entirely determined. Using the transformation (24), we need only compute equilibria for $S \equiv 1$.

For purely toroidal flow there is no constraint on the entropy and we may assume any relation $p = p(\Psi, \varrho)$. The most convenient relation is $p = T(\Psi)\varrho$, eq. (7), expressing the fact that due to the large heat conductivity along $\underline{B}$ the temperature is constant on a flux surface.

For this model the Bernoulli-type equation (18) reads

$$H(\psi) = -\frac{\Omega^2(\psi)}{2|\nabla\theta|^2} + T(\psi)\ln\varrho \qquad (27)$$

If we introduce

$$H_0 = \frac{H}{T} + \ell_n T \quad \text{and} \quad \Omega_0 = \frac{\Omega}{\sqrt{T}} \tag{28}$$

we obtain

$$H_0(\psi) + \frac{\Omega_0^2}{2|\nabla\theta|^2} = \ell_n \rho$$

and further

$$\rho = e^{H_0 + \Omega_0^2/2|\nabla\theta|^2} \tag{29}$$

The differential equation reads

$$\nabla\left[|\nabla\theta|^2 \nabla\psi\right] + |\nabla\theta|^2 F \frac{dF}{d\psi} + \rho\left[\frac{\Omega_0}{|\nabla\theta|^2}\frac{d\Omega_0}{d\psi} + \frac{dH_0}{d\psi}\right] = 0 \tag{30}$$

or

$$\nabla\left[|\nabla\theta|^2 \nabla\psi\right] + |\nabla\theta|^2 F \frac{dF}{d\psi} + \frac{dp}{d\psi} = 0 \tag{30a}$$

This equation has the form of the Grad-Schlüter-Shafranov equation with arbitrary profiles F, Ω_0, H_0 and a free function $T = T(\psi)$ in the transformation (28).

II. Numerical Method

In the plasma region Γ the differential equation (19b) has to be solved together with the algebraic equations (17b) and (18b). The five functions Φ, Ω, I, H and S depending only on Ψ can be arbitrarily specified. For purely toroidal flow the temperature is introduced instead of the entropy and eq. (30) is to be solved for given F, Ω_0 and H_0. The plasma cross-section can be specified, leading to the boundary condition

$$\Psi = \text{ct.} \quad \text{on the surface} \quad \partial\Gamma \tag{31}$$

With the definition

$$k = \left(1 - \frac{\Phi^2}{S}\right) |\nabla\Theta|^2 \tag{32}$$

we keep the highest derivatives in eq. (19b) or 30 explicitly and abbreviate the other terms by G

$$\nabla [k \nabla\Psi] + G = 0 \qquad \text{in} \quad \Gamma \tag{33}$$

$$\Psi = g_1 \qquad \text{on} \quad \partial\Gamma_1$$

$$\frac{\partial\Psi}{\partial n} = g_2 \qquad \text{on} \quad \partial\Gamma_2 \tag{34}$$

$$\partial\Gamma = \partial\Gamma_1 \cup \partial\Gamma_2$$

The boundary conditions can be generalized to Dirichlet and v. Neumann conditions.

The Galerkin method uses a linear expansion for Ψ and solves eq. (33) in its weak form. We work with two-dimensional finite elements as expansion functions:

$$\Psi = \sum \alpha_i h_i (r,z) \tag{35}$$

The elements h_i are chosen to satisfy the Dirichlet boundary condition. There then is no error associated with this condition. Integration by parts yields the matrix equation for the vector $\underline{\alpha}$ of the expansion coefficients /5-7/:

$$\underline{\underline{K}}\,\underline{\alpha} = \underline{b} \tag{36}$$

where $\underline{\underline{K}}$ denotes the stiffness matrix and $\underline{b}$ the force vector:

$$K_{ij} = \int_\Gamma k \nabla h_i \nabla h_j \, d\tau \tag{37}$$

$$b_j = \int_\Gamma G h_j \, d\tau + \int_{\partial\Gamma_2} k g_2 h_j \, d\tau + X_j$$

where X_j expresses the known value of Ψ along $\partial\Gamma_1$:

$$X_j = \int_{\partial\Gamma_1} \sum_i \hat{\alpha}_i k \nabla h_i h_j \, dS \tag{38}$$

The most common two-dimensional finite elements are triangular and rectangular elements with initially straight-line boundaries. However, the development of the variable 4 to 8 - node isoparametric elements has given the method much more flexibility; for details see Ref. /5-7/. We prefer rectangular elements because they yield more accurate results than triangular ones /6/. In addition, the rectangular elements are better suited to represent the flux contours. Our code is an extension of the existing finite-element code for heat transfer, Ref. /8-10/. This code is based on earlier work of Wilson, Ref. /11,12,5/, and is described in Ref. /13/.

Isoparametric mapping provides a one-to-one correspondence between the local (s,t) and global (r,z) coordinates (see Fig. 1). The coordinate transformation between the bi-unit square and the curvilinear element is given by

$$r_m(s,t) = \sum_{i=1}^{8} h_{im}(s,t)\, r_{im}$$
$$z_m(s,t) = \sum_{i=1}^{8} h_{im}(s,t)\, z_{im} \tag{39}$$

where (r_{im}, z_{im}) are the global coordinates of node i in element m and h_{im} is the interpolation function corresponding to node i of element m. The interpolation functions are defined as follows:

$$h_1 = \frac{1}{4}(1+s)(1+t) - \frac{1}{2}h_5 - \frac{1}{2}h_8$$

$$h_2 = \frac{1}{4}(1-s)(1+t) - \frac{1}{2}h_5 - \frac{1}{2}h_6$$

$$h_3 = \frac{1}{4}(1-s)(1-t) - \frac{1}{2}h_6 - \frac{1}{2}h_7$$

$$h_4 = \frac{1}{4}(1+s)(1-t) - \frac{1}{2}h_7 - \frac{1}{2}h_8$$

$$h_5 = \frac{1}{2}(1-s^2)(1+t) \tag{40}$$

$$h_6 = \frac{1}{2}(1-s)(1-t^2)$$

$$h_7 = \frac{1}{2}(1-s^2)(1-t)$$

$$h_8 = \frac{1}{2}(1+s)(1-t^2)$$

where the local coordinates (s,t) vary in the interval (-1,1). If the curvilinear element has one or more straight sides, the midside node numbers 5, 6, 7 or 8 corresponding to the straight sides can be omitted by setting the corresponding interpolation functions equal to zero.

The same interpolation functions are used to approximate the flux Ψ within the element in terms of the value at nodes 1 to 8:

$$\Psi_m(s,t) = \sum_{i=1}^{8} h_{im}(s,t)\,\alpha_{im} \tag{41}$$

where α_{im} is the value of Ψ at the i^{th} nodal point of element m. The determinant of the transformation is

$$J_m = \frac{\partial r}{\partial s}\frac{\partial z}{\partial t} - \frac{\partial z}{\partial s}\frac{\partial r}{\partial t} \tag{42}$$

The derivatives give

$$\begin{pmatrix} \frac{\partial \Psi}{\partial r} \\ \frac{\partial \Psi}{\partial s} \end{pmatrix} = J_m^* \begin{pmatrix} \frac{\partial \Psi}{\partial s} \\ \frac{\partial \Psi}{\partial t} \end{pmatrix} \tag{43}$$

$$J_m^* = \frac{1}{J_m} \begin{pmatrix} \frac{\partial z}{\partial t} & -\frac{\partial z}{\partial s} \\ -\frac{\partial r}{\partial t} & \frac{\partial r}{\partial s} \end{pmatrix} \tag{44}$$

The matrix elements K_{ij} , eq. (37), and the force vector $\underline{b}$, eq. (38), are evaluated in "natural" s,t coordinates for each element individually by means of eqs. 39-44. The integration is performed by Gaussian quadratures. We emphasize that the stiffness matrix $\underline{\underline{K}}$ for $\Phi^2/\varrho < 1$ is positive definite and of symmetric band form. Efficient solution techniques for the linear system used to solve eq. 36 can be applied, these requiring a minimum amount of storage and computing time /14/. On the other hand, a finite difference solution for our problem, eq. 33, produces a non-symmetric matrix - a complication additional to the problem of handling the boundary conditions.

The equilibrium equation (33) is highly non-linear and requires an iteration for the numerical solution. We apply the Piccard iteration in the form

$$\nabla\left[k(\Psi^n)\,\nabla\Psi^{n+1}\right] + G(\Psi^n) = 0 \,, \qquad (45)$$

where the index n denotes the value of the nth iteration, as in Ref. /15/. Please note that the relation between ϱ and Ψ, eq. 18b, has to be found numerically, i.e. $\varrho = \varrho(r, \Psi^n, |\nabla\Psi^n|^2)$. If the flow is purely toroidal the stiffness matrix is independent of Ψ. Thus $\underline{\underline{K}}$ needs only be inverted once.

The plasma boundary can be specified arbitrarily, e.g. pointwise. From these boundary points and a chosen central point we create a net of rectangular elements, the innermost ones being degenerated to triangles, as is shown in Fig. 2. As first applications we compute equilibria with

up-down symmetry leading to a Dirichlet condition on the surface and to a v. Neumann condition along the z = 0 plane. The code is, of course, not restricted to such geometries. The plasma behaviour is quite anisotropic with respect to directions along the magnetic field and across it. For an accurate numerical description of stability and transport it is necessary to use Ψ as a coordinate. The spectral codes for linear MHD stability, PEST /16/ and ERATO /17/, work in special flux coordinates and the mapping of the equilibrium into flux coordinates is an important part of the code. Formulation of the equilibrium problem directly in flux coordinates involves - owing to the singularity at the origin - severe numerical problems, which were recently overcome by using a global Fourier expansion in the angle /18, 19/. Our method shifts the mesh points in the iteration to coincide with surfaces Ψ, ϑ = ct., with ϑ being the poloidal angle of the surface points to the magnetic axis - but still works in cylindrical coordinates. It is easy to transform from the poloidal angle ϑ to an angle $\hat{\vartheta}$ with straight field lines. It has been pointed out by Grad /20/ that the geometry converges faster than the function Ψ. In this fashion our code is able to provide very accurate equilibrium data in Ψ, ϑ, θ (or $\Psi, \hat{\vartheta}, \theta$) coordinates efficiently as input for ideal MHD spectral /17/ or resistive stability /21/ codes.

III. Results

A) Static Equilibria

The first applications of the code serve to test its accuracy. The behaviour of ψ near the magnetic axis computed using linear and quadratic elements is examined in detail. An Expansion of ψ begins with quadratic terms

$$\psi = e\, x^2 + 1/e\, z^2 + \ldots$$

where x denotes the radial distance from the magnetic axis and e is the half-axis ratio. We may expect that the bi-linear elements yield an inaccurate representation. A very simple equilibrium , specified by the profiles in eq. (30 a)

$$\frac{dp}{d\psi} = -c_1 \quad \text{and} \quad F\frac{dF}{d\psi} = d_1 \tag{46}$$

is taken. The surface is defined by the analytic representation

$$\begin{aligned} r &= A + \cos\left[\beta + \delta \cdot \sin\beta\right] \\ z &= K \sin\beta \end{aligned} \tag{47}$$

with up-down symmetry imposed and hence $o \leq \beta \leq \pi$.
The values of the parameters are $c_1 = 2.o$, $d_1 = o.5 \cdot R_o^2$, $K = 2.5$, $\delta = o.45$ and $A = 3.o$.

This curve is the outermost contour in Figs. 2a and 2b. The mesh of finite elements is constructed from this

curve and an arbitrary inner print on the z=o axis, R_o. For the 4-node, bilinear elements, shown in Fig. 2a, R_o has the value R_o=2.5 and for the 8-node, bi-quadratic elements, shown in Fig. 2b, the value is R_o=R(axis)=3.2o. The number of radial and poloidal mesh points is 15, NR = NP = 15. The 8-node elements coincide with flux contours, which are defined with equidistant values

$$\xi_i = \left[(\psi_i - \psi_s)/(\psi_a - \psi_s) \right]^{1/2} , \quad i = 1,2, \ldots, NR$$

where ψ_a (ψ_s) is the value of ψ at the axis (surface). This mesh is rearranged in the iteration procedure until convergence for the flux function and the mesh is obtained. Both choices of the finite elements yield almost identical results, even if the origin of the finite-element net, R_o , is initially chosen far away from its final value, as is the case in Fig. 2a. Good results are also obtained for the combinations of linear and quadratic elements (6-node elements). This conclusion holds, in addition, for the more complicated current profiles discussed later on. We prefer, usually, the 8-node elements, since a given surface is then better represented. Linear elements underestimate the arc length of a flux contour yielding thus an inaccurate value for the safety factor, which has to be compensated by a larger number of elements.

The next test case is a comparison with an equilibrium computed by the Garching code /15/. The surface is speci-

fied by the parameters K=1.5, δ=o and A=3.o in eq.(47) yielding an aspect ratio of three. The profiles are parabolic ones and given by

$$p = c_1 (\psi - \psi_s)^2 \quad \text{and} \quad F = 1 + d_1 (\psi - \psi_s)^2 \qquad (48)$$

with $c_1 = 1.26 \cdot 10^{-2}$ and $d_1 = 3.92 \cdot 10^{-2}$.

Then the magnetic axis is found at $R_a = 3.1o5$ and the elongation of the flux surfaces around the axis is $e = 1.36$. Fig. 3a displays the flux contours of the converged solution and Fig. 3b the toroidal current in dependence of the radius along the midplane.

The agreement between the results from the two different codes is very satisfactory. The error is of the order of 10^{-6} and, therefore, the comparison is not persued further. It is interesting to have a closer look on the convergence properties of our finite element code. Without mesh rearrangement the convergence is fast. After ten iterations the error - defined as the maximum value of the difference of two subsequent iterations

$\varepsilon^{(n)}(\psi) = \max \mid \psi_i^{(n)} - \psi_i^{(n-1)} \mid / (\psi_a - \psi_s)$ - is less than 10^{-5} as is seen in Fig. 4. The finite elements are rearranged during the first n_i (in this case n_i=3) iterations and then in steps of n_D (here n_D=3). The iteration is initialized with a constant current. Therefore, the error of the mesh -

$\varepsilon^{(n)}(\text{mesh}) = \max \{(r_i^{(n)} - r_i^{(n-1)}), (z_i^{(n)} - z_i^{(n-1)})\}/R_a^{(n)}$ - increases in the second iteration, but decreases then

monotonically to a value below 10^{-4}. The mesh rearrangement introduces an error in ψ, which is seen in the maxima of $\varepsilon(\psi)$ in Fig. 4. But in the subsequent iterations the error decreases substantially and is smaller than 10^{-4} at the end of the run. These local maxima in $\varepsilon(\psi)$ are possibly due to the linear interpolation used for convenience in the determination of the flux contours. The new mesh points are obtained as a superposition of old and new values, e.g.

$$r_i^{(n)} = \alpha\, r_i^{(n)} + (1-\alpha)\, r_i^{(n-1)}$$

to avoid oscillations of the magnetic axis. For the specific case discussed the constant is $\alpha = 0.75$. The values of the local maxima and minima of $\varepsilon(\psi)$ occurring in the course of iterations are decreased by a factor of 4 if the number of mesh points is doubled (NR=NP=41). The local minima can be made smaller by enlarging the stepsize for the renewing of the mesh, e.g. $n_D = 4$. The basic result is that the equilibrium is obtained in flux coordinates and is computed with sufficient accuracy. The number of iterations necessary for such an equilibrium is about two to three times larger than that for a case with fixed mesh.

Equally good results are obtained for a high beta-poloidal equilibrium ($\beta_p = 1.8$) taken from the study in Ref./22/. The surface is defined by the parameters K=1.65 and $\delta = 0.25$ in eq.(47) and an aspect ratio of 3.5.

The profiles have the form

$$\frac{dp}{d\psi} = - c_o \left(c_1(\psi - \psi_s) + c_2 (\psi - \psi_s)^2 \right)$$
$$F \frac{dF}{d\psi} = d_o \left(d_1 \cdot R_a^2 (\psi - \psi_s)^2 + d_3 (\psi - \psi_s)^4 \right) \qquad (49)$$

with constants $c_o=d_o=o.92$, $c_1=1.o$, $c_2=d_2=2.2o5$ and $d_3=o.$ The magnetic axis is then at $R_a = 3.8$. The flux contours of this equilibrium are displayed in Fig. 5a and the toroidal current in dependence of the radius along the midplane in Fig. 5b.

A divertor experiment like ASDEX separates the plasma by a "magnetic limiter" from the wall and avoids thereby the contact of the plasma with a material limiter. The corresponding equilibrium has a stagnation point on the plasma surface. At such an x-point the flux surface forms an angle of 90^o. A finite element code can easily represent the surface. As illustration an equilibrium from the ASDEX-UPGRADE design (Ref./23/) is computed. The surface is specified point-wise and the aspect ratio is three. Interpolating these points the surface can be represented with any desired number of poloidal points. In Fig. 6 the surface is plotted with 33 points. The profiles are the same as used in the previous case, eq. (49). Fig. 6 displays the flux contours for the converged equilibrium for equidistant values of $\sqrt{\psi}$. It is possible to shift the finite elements closer to the separatrix if a better resolution is needed without increasing the number of mesh points.

By construction the flux contour has an angle of exactly 90^{o} at the stagnation point yielding a value of $|\nabla\psi| = o$ there. Then the safety factor on the surface has an infinite value. This limit is approximated by any finite value on the nearest surface if the finite elements are accumulated sufficiently close to the surface. This yields the very accurate profiles needed as input for the stability code, Ref./21/, if the influence of the separatrix on the stability of tearing modes is to be analyzed. It has been found by the authors that a finite difference code cannot represent the separatrix well, even if a large number of points is taken.

B) Configurations With Steady Flow

The code is now applied to compute plasma states with flow. As pointed out above a purely toroidal flow does not change the type of the equilibrium equation - see eq. (30a). Analytic solutions can be obtained for a special choice of Ω_o, H_o and F, e.g. in Ref./24/ Ω_o is a constant and p and F^2 are linear in $\psi - \psi_s$ Since this solution is still complicated and requires numerical evaluation the comparison is not persued. More interesting is the result for the shift of the center of a surface, obtained by a large aspect ratio expansion. Similar expression are also derived in Refs. /2,19/.

This enhanced shift of the flux surfaces is reproduced by our numerical results. In the first application we take the constant current profile of eq. (46) with values for c_1 and d_1 as above and add a constant toroidal flow

$$\Omega_o = \omega_o / R_a \tag{50}$$

The function H_o is chosen such that

$$e^{H_o} = p(\psi, \Omega_o = o) = c_1(\psi - \psi_s) \tag{51}$$

Then the toroidal flow contributes only in the exponential term in eq. (30a). With increasing value ω_o the magnetic axis of the steady flow configurations is shifted more outwardly. The flux contours for the case of large toroidal flow, $\omega_o = 1.0$, are shown in Fig. 7. The comparison with the static case in Fig. 2a yields the enhanced shift of the flux surfaces. The dependence of the normalized shift $D = 1 - R_a(0)/R_a(\Omega)$ on the flow velocity is shown in Fig.9. The shift is more pronounced the smaller the elongation of the plasma in agreement with the analytical results. In Fig. 9 the shift for $K = 2.5$, 1.0 and 0.4 is plotted, where the other parameters are held fixed (e.g. $\delta = 0.45$). More realistic is the parabolic current profil of eq. (48). Again the function H_o is chosen to reproduce the pressure of the static case, i.e.

$$e^{H_o} = c_1(\psi - \psi_s)^2 \tag{52}$$

and the constants c_1 and d_1 have the above values and the toroidal flow is kept constant. The flux contours for the configuration with $\omega_o = 1.1$ is presented in Fig. 8. The corresponding static equilibrium is found in Fig. 3a. The shift of the magnetic axis in dependence of the flow velocity is plotted in Fig. 9. The detailed comparison with analytic results is presently persued. The profile studies have been extended to parabolic flow profiles. To facilitate the reproduction of experimental data the profiles are specified pointwise and then interpolated by cubic splines.

C) Storage And Time Requirements

The size of memory needed by the code is, basically, determined by the stiffness matrix eq.(37). The technique for storing the matrix $\underline{\underline{K}}$ and for solving the system of linear equations is adopted from the DOT code Ref./13/, where only the non-zero elements are processed. Therefore, keeping 400 000 words in the memory of the computer is sufficient for handling up to 81 radial and poloidal grid points. The results discussed have been computed using 8-node elementswith a 4x4 Gaussian quadrature for the integration per element. We list in Table 1 the CPU time required for different mesh sizes yielding a quadratic dependence for the computing time in dependence of the mesh size. The number of iterations is held fixed with n=10. The stiffness matrix is inverted in each iteration, although it is required only if the mesh is rearranged. For comparison the order of the integration scheme is reduced to a two-point formula. It is found that the results are almost identical to those obtained by a four-point quadrature, the difference is of the order of 10^{-3} to 10^{-4}. The CPU time is then decreased by a factor of 1.6 for larger mesh sizes ($NR \geq 21$). This makes it evident that the computing time is not merely spent in the solution of the system of linear equations but equally in the evaluation of the matrix elements. A good performance is also achieved by

using 4-node elements, where a two-point Gaussian formula is adequate. Please note that the total number of mesh points with 4-node elements is larger than with 8-node elements.

The code can easily be organized to start with a 11x11 mesh and then interpolate and transfer the results for ψ and the flux coordinates to a finer grid like 21x21 and 41x41. Then only a few iterations are required for the large systems. To optimize further the stiffness matrix will be inverted only if the mesh is changed. Assuming that a 21x21 finite element net is sufficient for most applications (and a 41x41 net for the tearing mode stability analysis of the code /21/), we estimate that an accurate solution is computed after 20 iterations in 5 to 1o seconds (and in about 15 seconds, respectively) on the CRAY.

Table 1:

CPU time in seconds for the 4-node and 8-node elements for different mesh sizes NR=NP with 2x2 or 4x4 points per elements used for the integration. The number of iterations is always ten. NT denotes the total number of mesh points. The runs have been performed on the CRAY-1 of the IPP computing center.

NR = NP	4-Node El. NT	4-Node El. 2x2 Int.	8-Node El. NT	8-Node El. 2x2 Int.	8-Node El. NT	8-Node El. 4x4 Int.
11	111	1.1	86	0.7	86	1.4
21	421	4.5	321	2.7	321	5.4
31	931	10.7	7o6	6.7	7o6	12.9
41	1641	20.6	1241	13.5	1241	24.4
51	2551	34.9	1926	23.4	1926	41.0
61	3661	54.5	2761	38.7	2761	63.4

IV. Summary

The equilibrium equation which determines a steady state in ideal MHD theory has an elliptic characteristic if there is no flow, purely toroidal flow or only small poloidal flow. For sufficient large poloidal flow the equation becomes hyperbolic. The equilibrium is determined numerically by using the finite element method. Quadrilateral, isoparametric elements with four to eight nodes are applied. The mesh is rearranged in the iteration process to coincide with contours of constant flux yielding the equilibrium finally in flux coordinates. Good results are obtained with bi-quadratic (8-node) elements, but also the bi-linear (4-node) elements are acceptable. It should be interesting to implement 9-node elementswhich exhibits a true bi-quadratic dependence in s and t. This requires an additional point in the center of an element. Then the ψ = ct. surface are equally represented on every contour. The extension of our code to this case should be relatively easy. The test cases for static equilibria as well as the results for purely toroidal flow demonstrate the high accuracy of the code together with its fast execution. In the present version the plasma surface is held constant - a rigid,perfect conducting wall. The results for ASDEX-UPGRADE with a separatrix as the plasma boundary suggest that the external solution is equally important, since small changes in the position and magnitude of the external currents shift the

location of the x-point considerably. In order to make our code self-consistent we should add the computation of the vacuum solution. At present, the code is, basically, used as input for ideal and resistive stability studies, where the external flux is not needed.

The code incorporates the isoparametric representation of 4-node, 6-node- and 8-node elements, the handling of general boundary conditions and the storage and the solution of the matrix problem efficiently - in the fashion of the heat transfer code used already at IPP. An iteration starting from a coarse grid and then interpolating to a finer grid yields accurate results in about 1o seconds on the CRAY-1.

The accurate results obtained so far encourage us to tackle the equilibrium problem with poloidal flow. Then, in addition to the differential equation, two algebraic equations have to be solved. As long as the poloidal flow does not exceed a fraction of $\sqrt{\beta}$ of the Alfvèn speed this system is solvable without any new problem. Naturally, we begin the iteration without poloidal flow to obtain a first approximation for the mesh and for ψ. Then the poloidal flow is switched on in steps. If the poloidal flow velocity exceeds the discussed threshold interesting new numerical results - and problems - should occur !

Figure Captions:

Fig. 1 Two dimensional mapping of 4- to 8-node isoparametric mapping.

Fig. 2a Finite element net (NR=NP=15) with 4-node elements.

Fig. 2b Finite element net (NR=NP=15) with 8-node elements coinciding with flux contours.

Fig. 3a Finite element net (NR=NP=21) with 8-node elements coinciding with flux contours.

Fig. 3b Toroidal current in dependence of the radius along the axis z = o.

Fig. 4 Error of ψ, $\varepsilon(\psi)$, and of the mesh, ε(mesh), in dependence of the number of iterations n.

Fig. 5a Finite element net (NR=NP=21) with 8-node elements coinciding with flux contours.

Fig. 5b Toroidal current in dependence of the radius along the axis z = o.

Fig. 6 Finite element net (NR=NP=33) with 8-node elements coinciding with flux contours.

Fig. 7 Finite element net (NR=NP=21) with 8-node elements coinciding with flux contours for the profile of Fig.2a but with constant toroidal flow $-\omega_o=1.0$.

Fig. 8 Finite element net (NR=NP=21) with 8-node elements coinciding with flux contours for the profile of Fig.3a but with constant toroidal flow $-\omega_o=1.1$.

Fig. 9 Shift of the magnetic axis $D=1-R_a(0)/R_a(\Omega)$ in dependence of the toroidal flow for constant (———) and parabolic (----) current profile.

References

/1/ Courant R. and Friedrichs K.O. (1948) Supersonic Flow and Shock Waves, Vol.I, Interscience, New York

/2/ Zehrfeld H.P. and Green B.J. Nucl.Fus. 10,251(1970) Zehrfeld H.P. and Green B.J. Nucl.Fus. 12,529(1972)

/3/ Hameiri E. Phys.Fluids 26,230(1983)

/4/ Hameiri E. "Adiabatic Compression of Rotating Plasmas", Physical Review A, 27, 1259 (1983)

/5/ Bathe K.J. and Wilson E.L., Numerical Methods in Finite Element Analysis, Prentice-Hall, Inc., Englewood Cliffs, New Jersey (1976)

/6/ Zienkiewicz O.C., The Finite Element Method, Third Edition, McGraw-Hill, London (1977)

/7/ Hinton E. and Owen D.R.J., An Introduction to Finite Element Computations, Pineridge Press, Limited, Swansea, U.K. (1979)

/8/ Gorenflo H. and Jandl O., IPP 4/148, Max-Planck-Inst. für Plasmaphysik, Munich (1977)

/9/ Söll M., Jandl O. and Gorenflo H., IPP 4/142 Max-Planck-Inst. für Plasmaphysik, Munich (1976)

/10/ Gorenflo H. and Jandl O., IPP 4/167, Max-Planck-Inst. für Plasmaphysik, Munich (1978)

/11/ Wilson E.L., "A Digital Computer Program for the Steady-State Temperature Analysis of Plane or Axisymmetric Bodies", Aerojet-General Corporation, Sacramento, California, Report No. TD-44 (1965)

/12/ Wilson E.L. and Nickell R.E., "Application of the Finite Element Method to Heat Conduction Analysis", Nuclear Engineering and Design (Holland), Vol.4, pp.276-286(1966)

/13/ Polivka R.M. and Wilson E.L., "FE Analysis of Non-linear Heat Transfer Problems" (DOT) Report No. UC SESM 76-2, Department of Civil Engineering, University of California, Berkeley, California (1976)

/14/ Bathe K.J., Wilson E.L., Iding R.H., NONSAP, Report No. UC SESM 74-3, Dept. of Civil Engineering, Univ. of California, Berkeley, California (1974)

/15/ Lackner K. Comput.Phys.Comm. 12,33(1976)

/16/ Grimm R.C., Greene J.M. and Johnson J.L., Methods Comput.Physics 16,253(1976)

/17/ Gruber R., Troyon F., Berger D., Bernard L., Rousset S., Schreiber R., Kerner W., Schneider W. and Roberts K.V., Comput.Phys.Comm. 21,321(1981)

/18/ Lao L.L., Hirshman S.P. and Wieland R.M., Phys.Fluids 24,1431(1981)
Lao L.L., Wieland R.M. Houlberg W.A. and Hirshman S.P., Comput.Phys.Comm. 27,129(1982)

/19/ Lao L.L., W.A. Cooper, R.M. Wieland and F.J. Helton, GA Technologies Report GA-A17045, to be published

/20/ Grad H., Courant Inst. Report MF-93 (COO-3077-154), October 1978

/21/ Kerner W. and Tasso H., Comput.Phys.Comm. 24,407(1981)
Kerner W. and Tasso H., Phys.Rev.Letters 49,654(1982)
Kerner W. and Tasso H., in Plasma Physics and Controlled Nuclear Fusion Research (Proc. 9th Int. Conf. Baltimore, 1982, paper IAEA-CN-41/P -2-2

/22/ Gruber R., Schreiber R., Troyon F., Kerner W., Lackner K., Sykes A. and Wesson J., in Plasma Physics and Controlled Nuclear Fusion Research (Proc. 7th Int. Conf. Innsbruck, 1978), Vol. 1, IAEA Vienna (1979), 593

/23/ ASDEX Upgrade Project Team, ASDEX-UG Phase II, IPP 1/217, Max-Planck-Inst. für Plasmaphysik, Munich (Mai 1983)

/24/ Maschke E.K. and Perrin H., Plasma Physics 22,579(1979)

Acknowledgement

One of the authors (W.K.) wants to thank the colleagues at the MFD of the Courant Institute in New York for their hospitality during his visit in 1983, and especially, Drs. W. Grossmann and H. Weitzner for their constant support. We also thank E. Schwarz for her contribution to the development of the code.
This work was supported by the U.S. Department of Energy Contract No. DE-AC02-76ERO 3077.

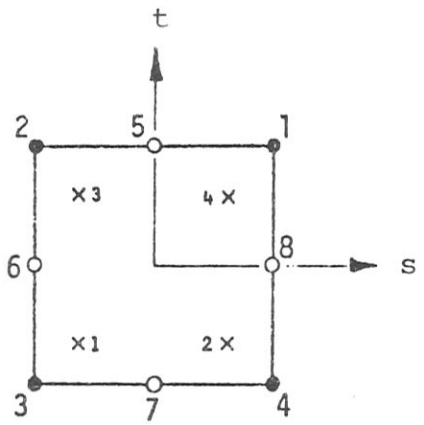

× Gauss Point Locations
for 2x2 Integration Order

(a) Bi-unit Square in
Local s-t System

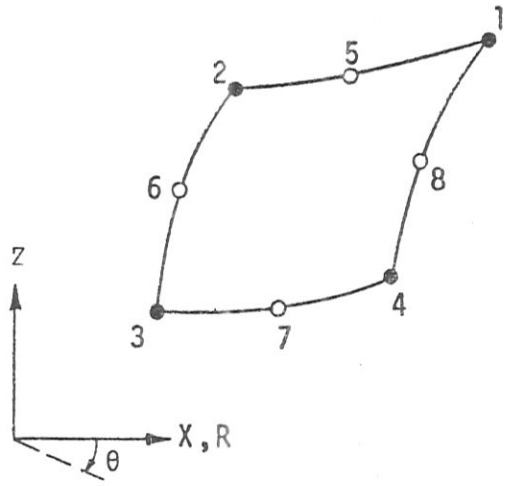

(b) Curvilinear Two-Dimensional
Element in Global X- System

FIG. 1 TWO-DIMENSIONAL MAPPING OF 4- TO 8-NODE ISOPARAMETRIC ELEMENT

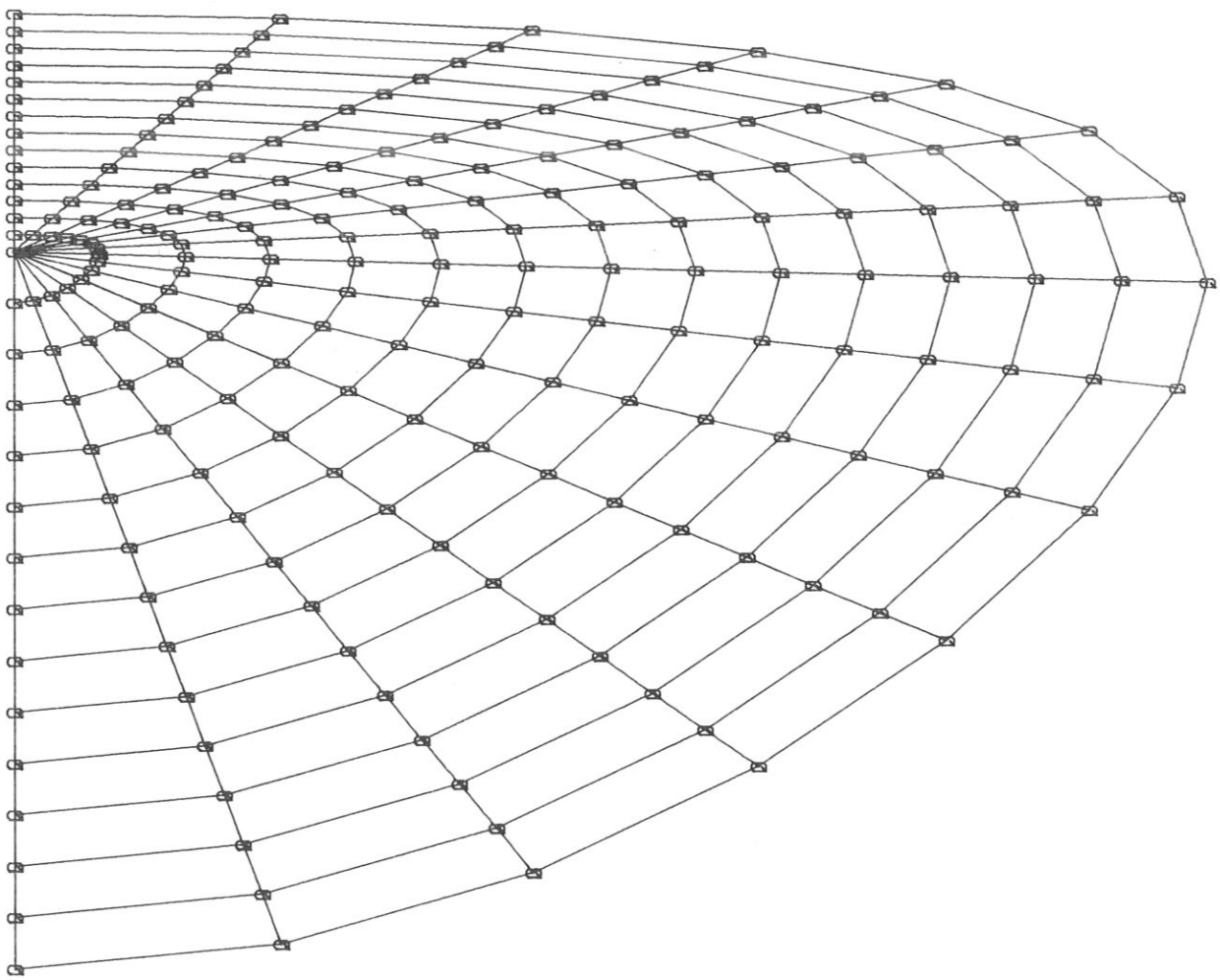

Fig. 2a

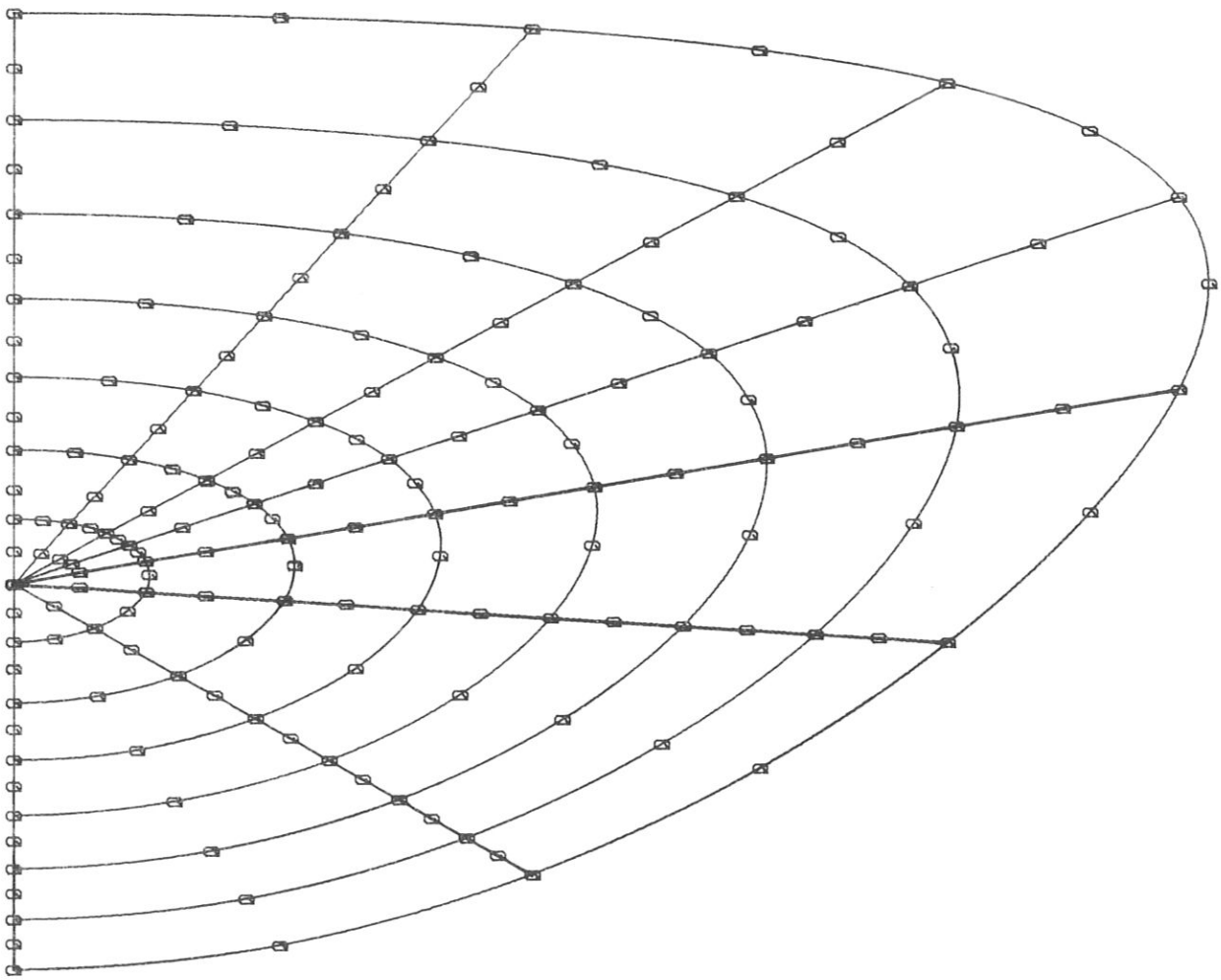

Fig. 2b

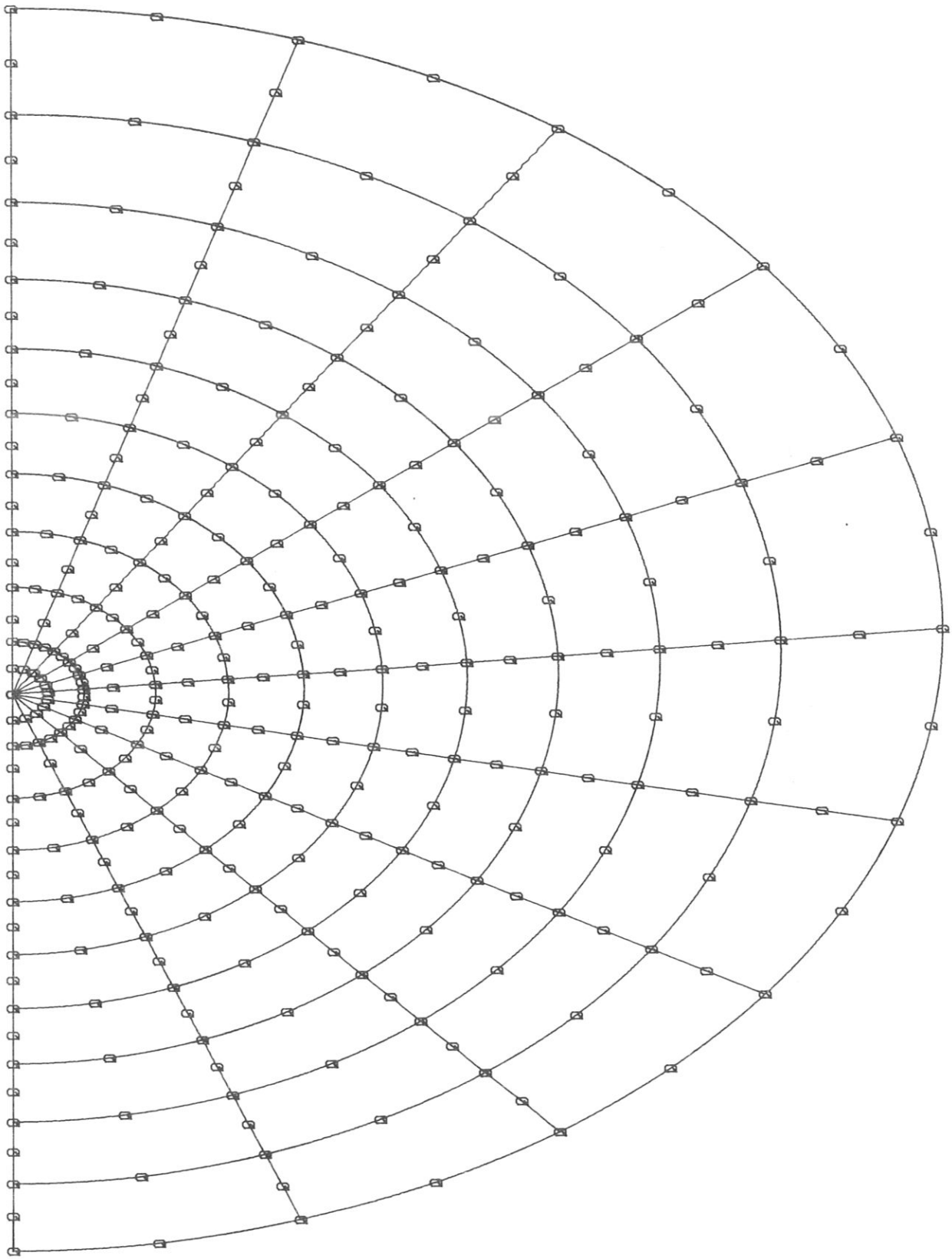

Fig. 3a

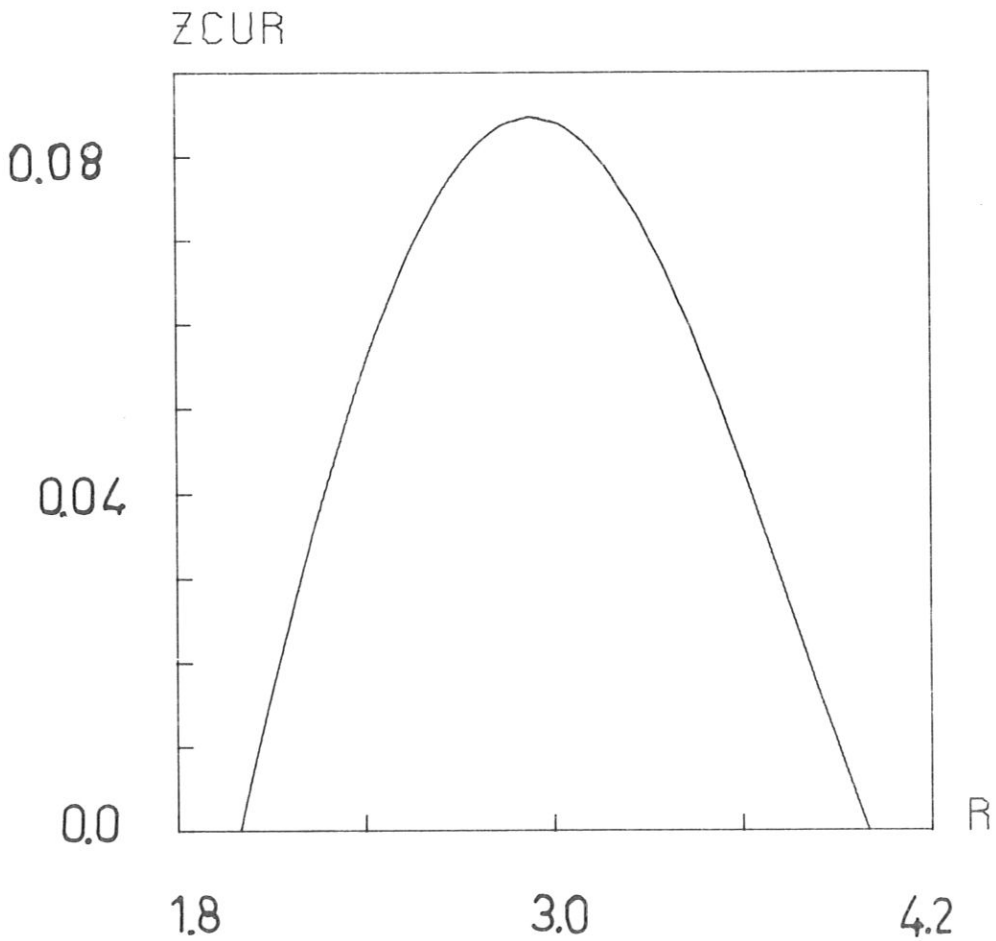

Fig. 3b

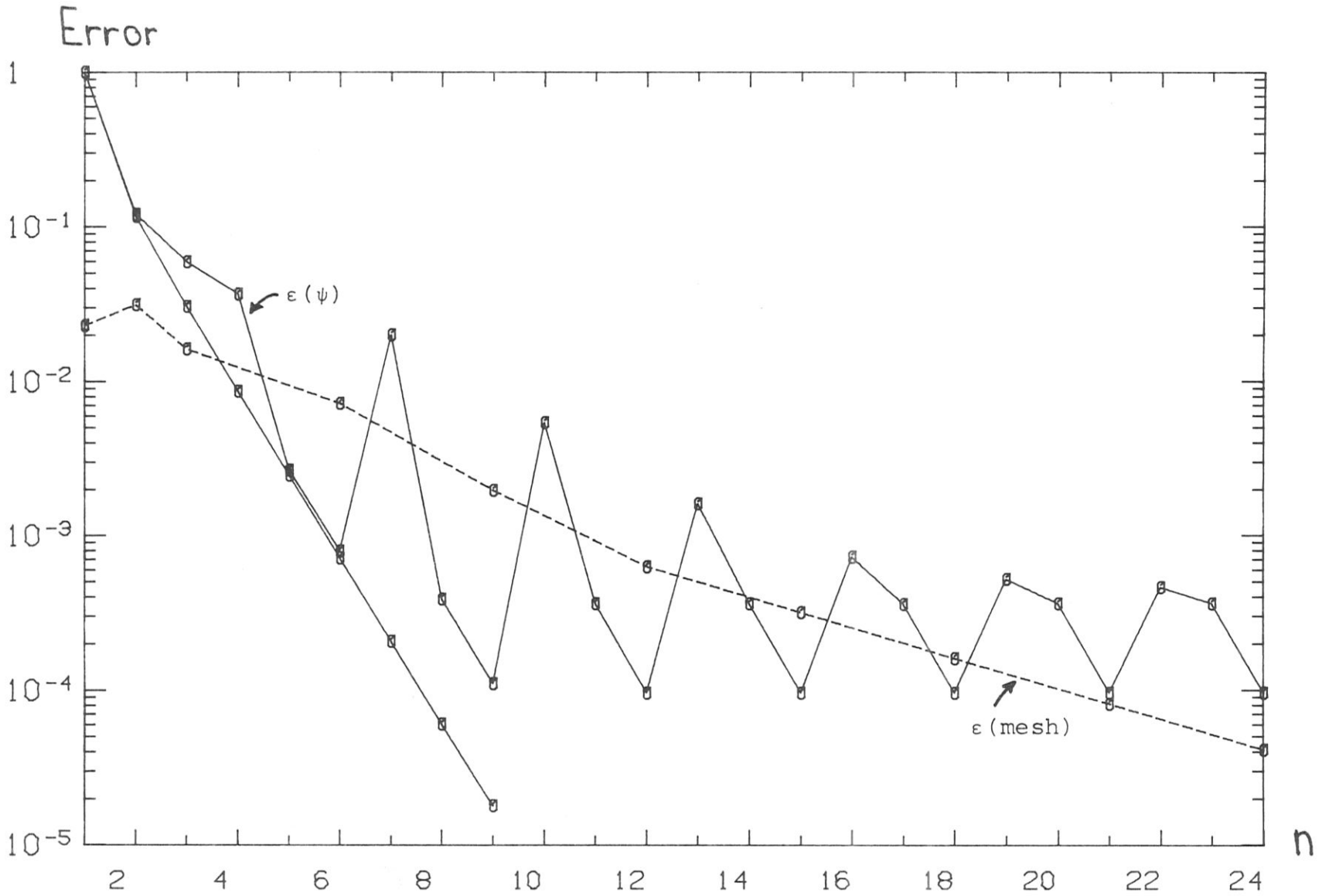

Fig. 4

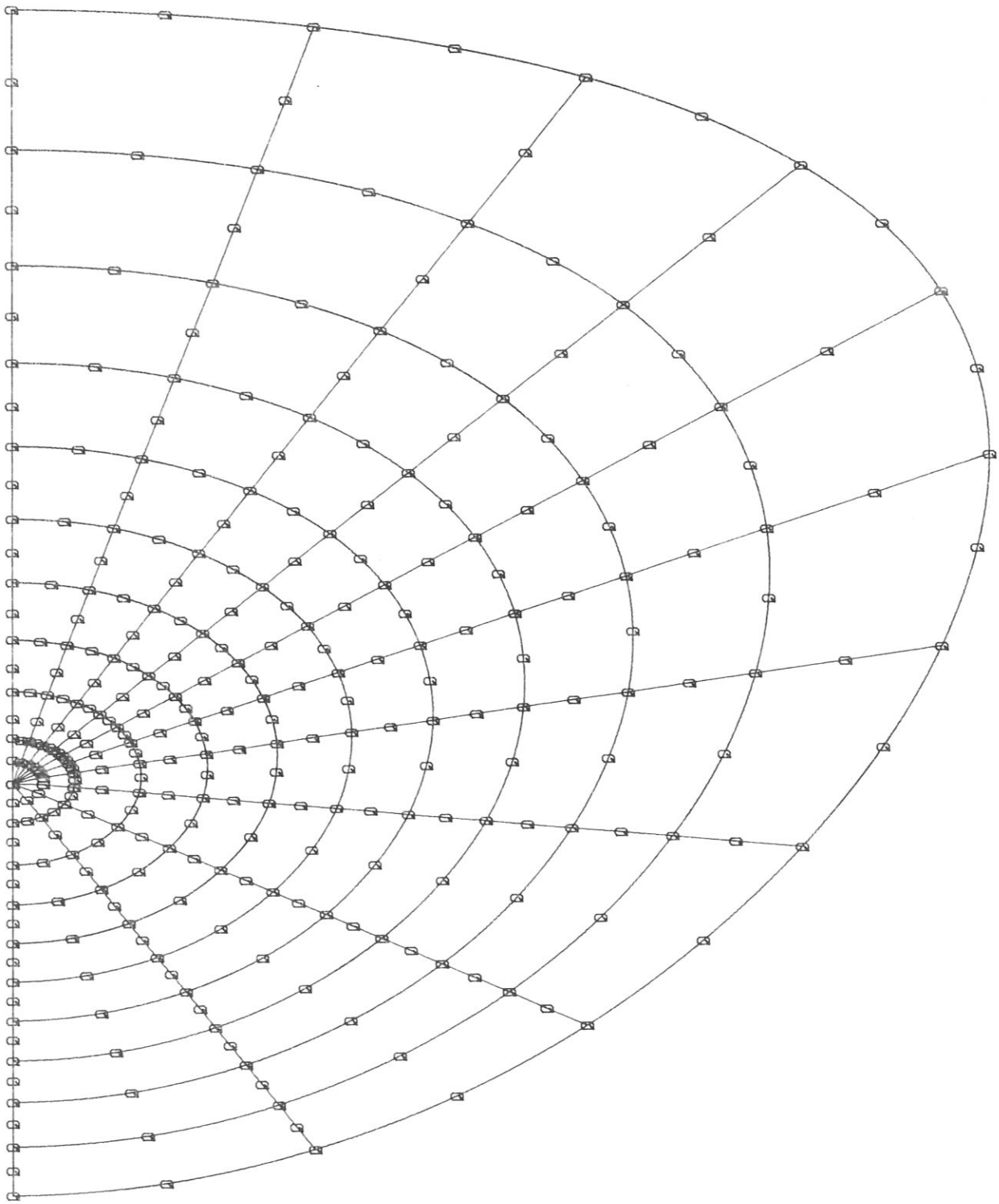

Fig. 5a

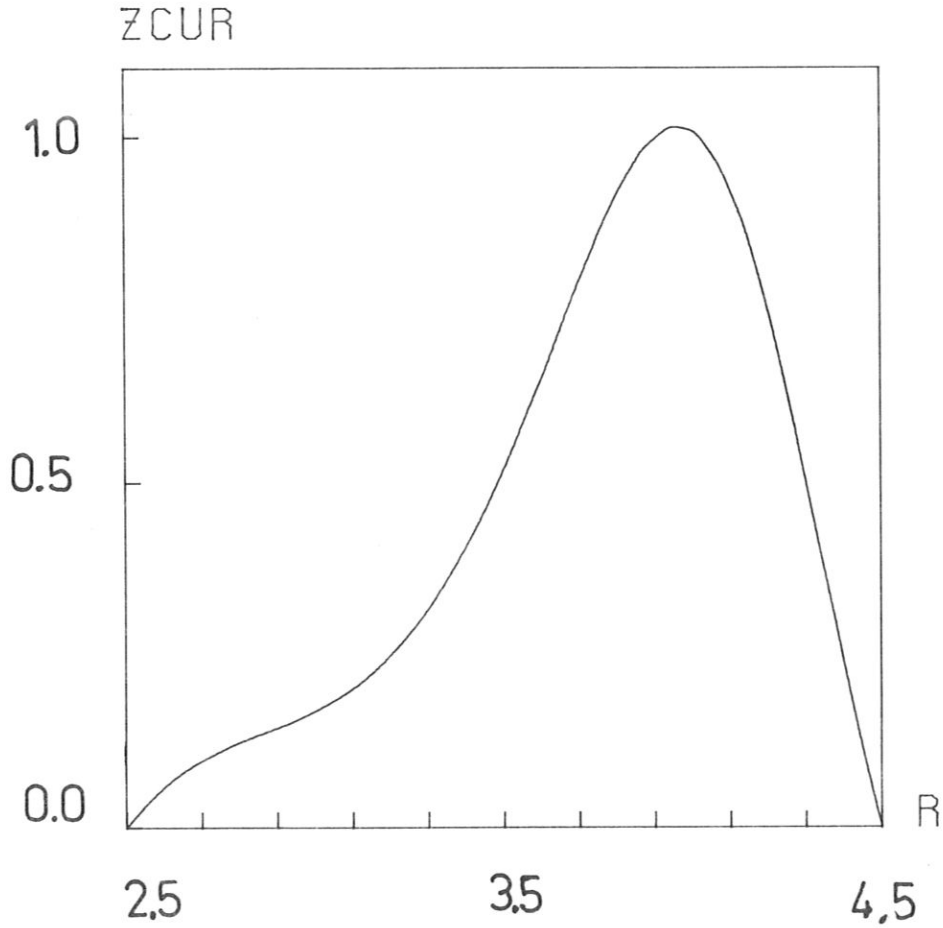

Fig. 5b

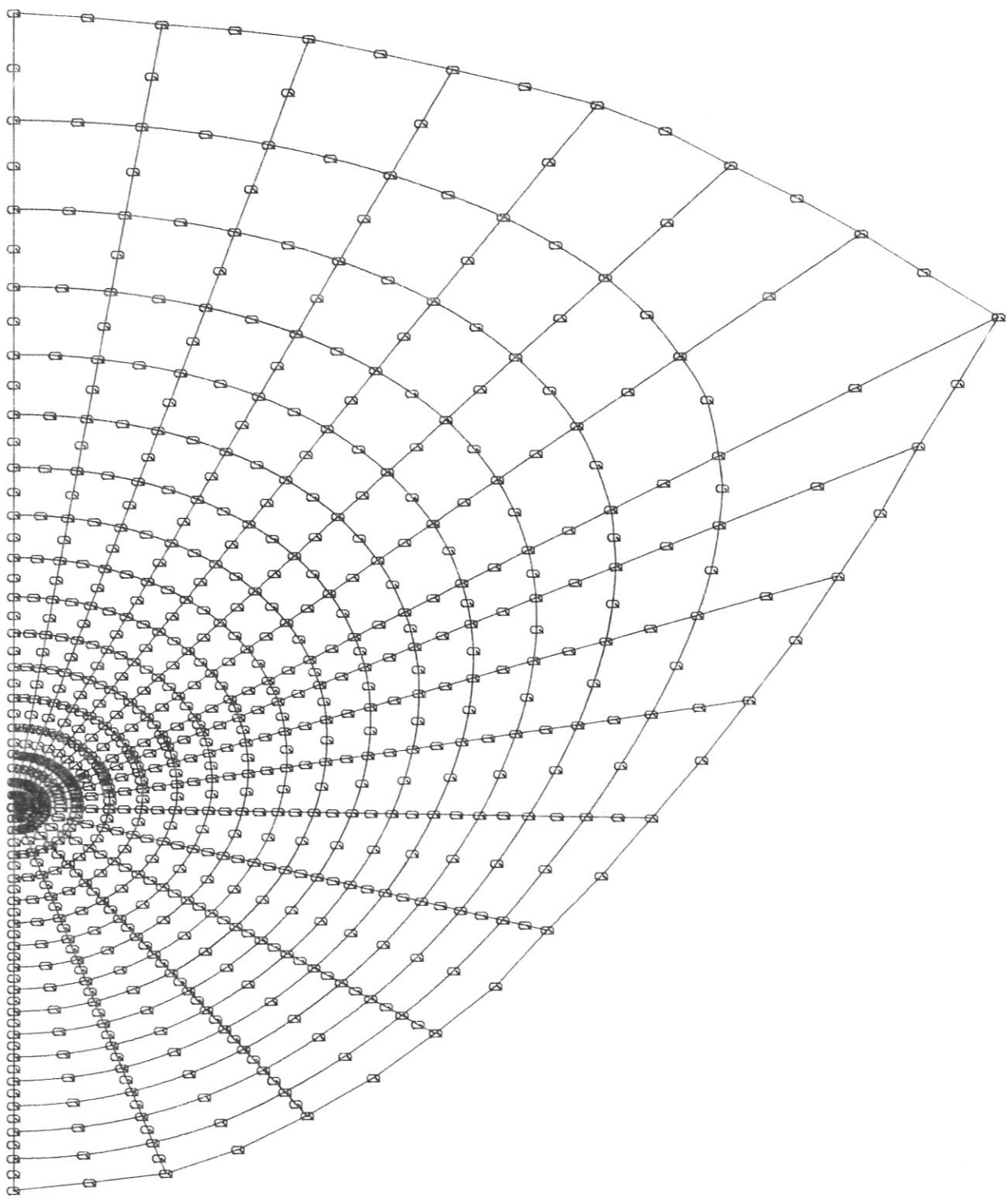

Fig. 6

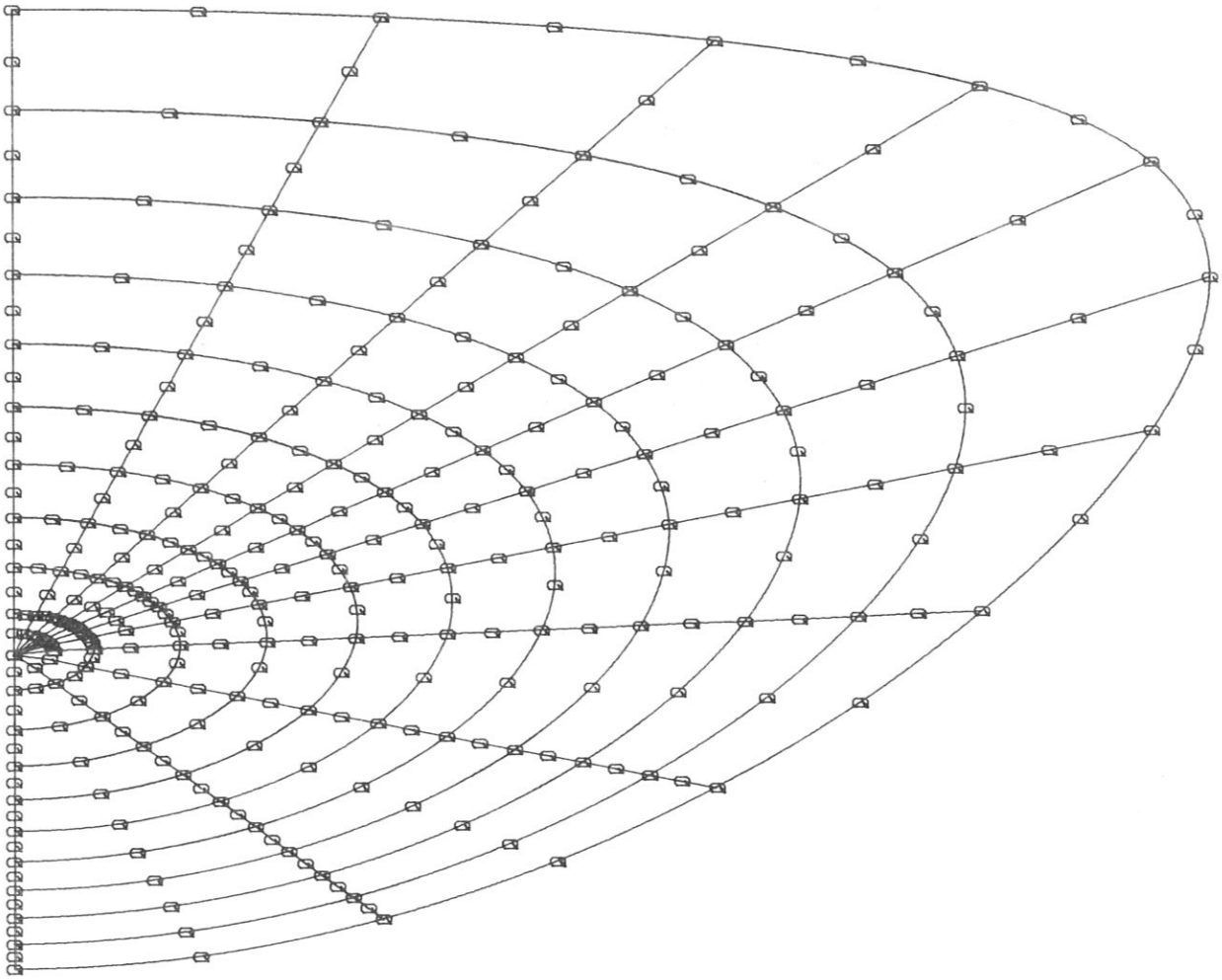

Fig. 7

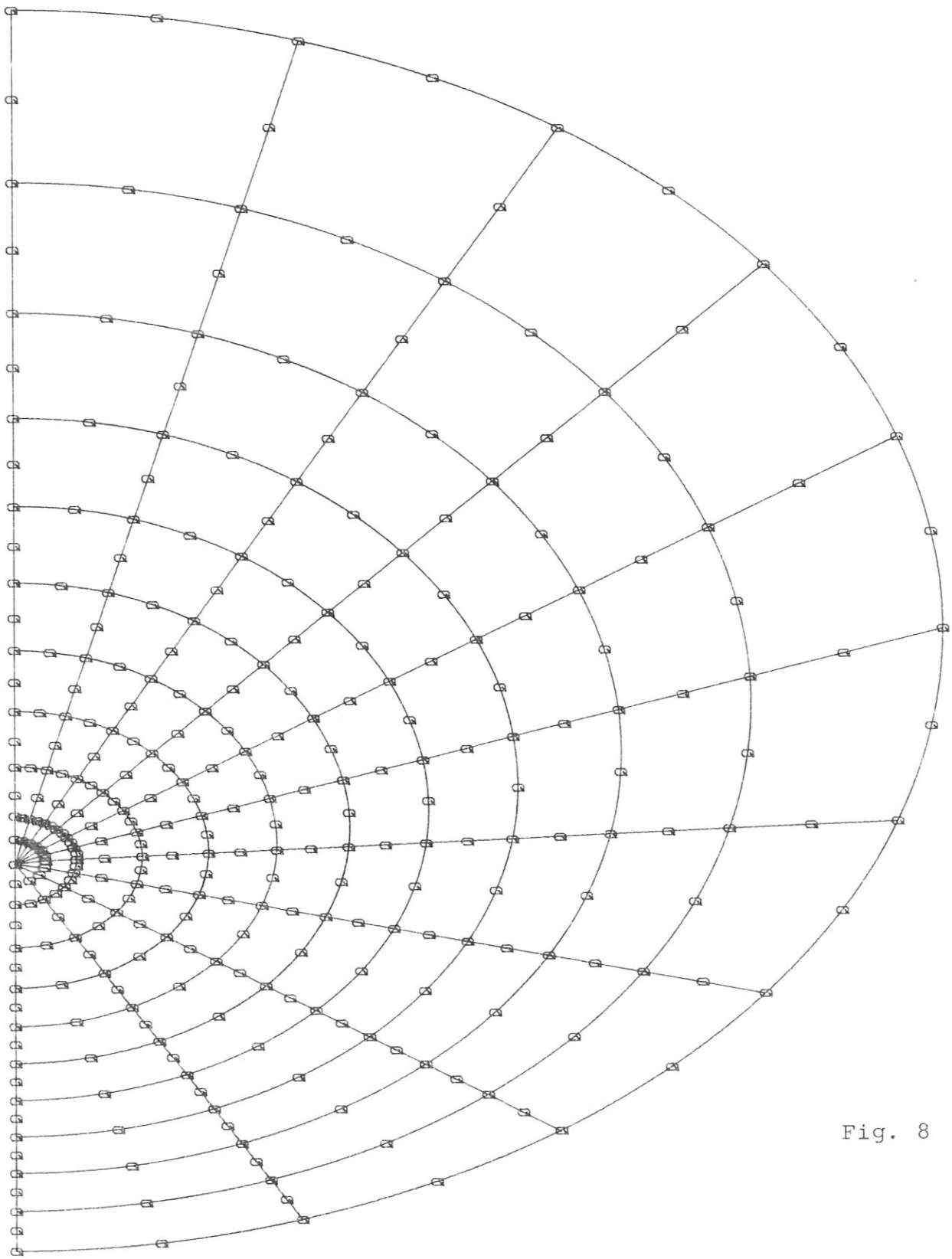

Fig. 8

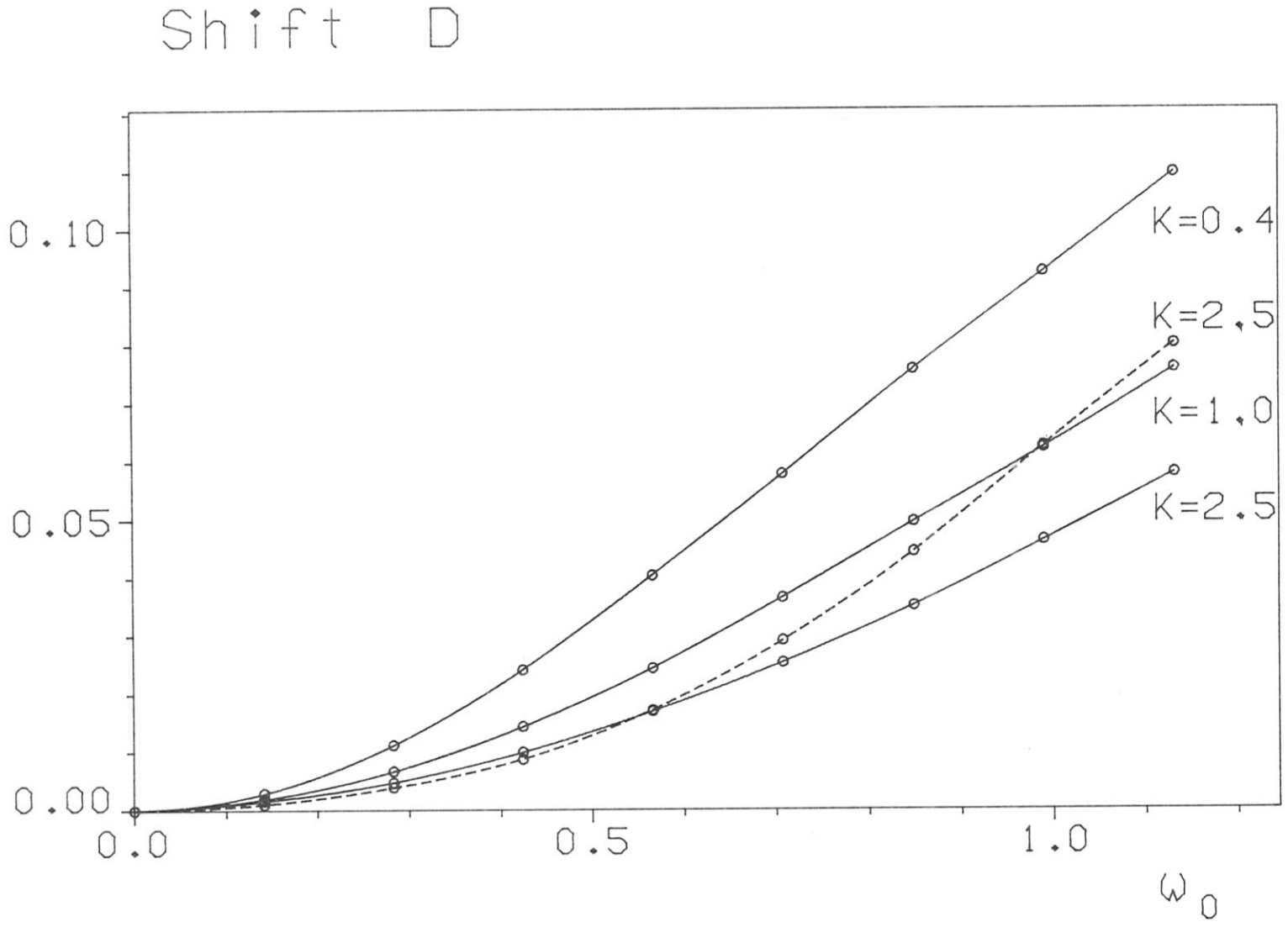

Fig. 9